Space, Time, and Learning in the Hippocampus:

How Fine Spatial and Temporal Scales Are Expanded into Population Codes for Behavioral Control

Anatoli Gorchetchnikov and Stephen Grossberg
Department of Cognitive and Neural Systems,
Center for Adaptive Systems
and
Center of Excellence for Learning in Education, Science and Technology
Boston University
677 Beacon St
Boston, MA 02215

November 7, 2006
CAS/CNS Tech Report # **CAS/CNS-TR-06-005**

Running head: Space, Time, and Learning in the Hippocampus

Pages: 23

Figures: 4

Tables: 3

Corresponding author: Stephen Grossberg, steve@bu.edu

Keywords: Spatial navigation, Adaptively timed learning, Grid cells, Place cells, Entorhinal Cortex, Dentate gyrus, CA3.

Abstract

The hippocampus participates in multiple functions, including spatial navigation, adaptive timing, and declarative (notably, episodic) memory. How does it carry out these particular functions? The present article proposes that hippocampal spatial and temporal processing are carried out by parallel circuits within entorhinal cortex, dentate gyrus, and CA3 that are variations of the same circuit design. In particular, interactions between these brain regions transform fine spatial and temporal scales into population codes that are capable of representing the much larger spatial and temporal scales that are needed to control adaptive behaviors. Previous models of adaptively timed learning propose how a spectrum of cells tuned to brief but different delays are combined and modulated by learning to create a population code for controlling goal-oriented behaviors that span hundreds of milliseconds or even seconds. Here it is proposed how projections from entorhinal grid cells can undergo a similar learning process to create hippocampal place cells that can cover a space of many meters that are needed to control navigational behaviors. The suggested homology between spatial and temporal processing may clarify how spatial and temporal information may be integrated into an episodic memory. The model proposes how a path integration process activates a spatial map of grid cells. Path integration has a limited spatial capacity, and must be reset periodically, leading to the observed grid cell periodicity. Integration-to-map transformations have been proposed to exist in other brain systems. These include cortical mechanisms for numerical representation in the parietal cortex. As in the grid-to-place cell spatial expansion, the analog representation of number is extended by additional mechanisms to represent much larger numbers. The model also suggests how visual landmarks may influence grid cell activities via feedback projections from hippocampal place cells to the entorhinal cortex.

Introduction

The multitude of seemingly independent behavioral functions carried out by the hippocampal system has attracted intense interest from researchers. Several of the most studied functions are the following: (1) The role of the hippocampal system in spatial navigation has been of special interest since O'Keefe and Dostrowsky (1971) showed the spatial correlates of pyramidal cell firing in the hippocampus. These cells tend to fire in a specific portion of the environment (place) independently of the head direction and movement speed, hence the term *place cells*. How place cells are formed has attracted even more interest since the recent discovery of grid cells (Hafting et al., 2005) within entorhinal cortical circuits that project to the hippocampus. (2) The role of the hippocampus in classical conditioning is limited to certain experimental paradigms that require temporal integration over a delay period; e.g., trace conditioning and sufficiently delayed non-matching to sample, and is crucial for adaptive timing of the conditioned response (Berger & Thompson, 1978; Eichenbaum, Otto, & Cohen, 1994). (3) Another function that was first highlighted by studies of patient HM (Scoville & Milner, 1957) is the role of the hippocampal system in declarative memory, especially in episodic memory. Eichenbaum et al. (1999) suggested that each episode in memory consists of a specific spatiotemporal combination of stimuli and behavior and discussed the evidence supporting this claim.

While these functions are often studied independently and in different species, there is no reason to believe that they are, in fact, independent. Spatial information and temporal information are crucial parts of an episode, and may be used to form an episodic memory. This paper focuses on hippocampal spatial and temporal processing and proposes that these are parallel computations performed within the same system by circuits that are sufficiently homologues to be considered variations of the same design.

Space and Time in Homologous Circuits. The adaptive timing model of Grossberg and colleagues (Grossberg & Merrill, 1992, 1996; Grossberg & Schmajuk, 1989) proposed how the dentate gyrus (DG) and hippocampal field CA3 may interact to learn adaptively timed behavioral responses (e.g., Gibbon, 1991; Roberts, Cheng, & Cohen, 1989; Smith, 1968) and neurophysiological cell activations (Berger, Berry, & Thompson, 1980; Berger, Laham, & Thompson, 1986; Hoehler & Thompson, 1980) during classical and instrumental conditioning. Here we introduce a model of spatial processing that describes how the same DG-CA3 circuits may also learn place fields for spatial localization. Grossberg et al. proposed a circuit to bridge a temporal interval that can span up to several seconds, and showed how this circuit could learn to adaptively time responses within this interval. A homologous spatial circuit is described herein that can similarly expand the range of positions and distances that can be represented, up to many meters, but instead of providing the information in the form of "now is the time…," it signals that "here is the place…"

The spatial case is in general more complex than the temporal, but it is more easily compared with the latter by the following simplifying assumptions. First, assume that the spatial environment is one-dimensional. Second, assume that the movement always proceeds in one direction. Finally, assume that the movement speed is constant. Under these assumptions, the spatial position of the animal is linearly dependent on time from the trial onset. Experimental evidence supports the link between time and spatial properties of place cells. For example, Redish et al. (2000) has shown that the elapsed time since leaving the start box on the 1D linear track is a good predictor of the place field realignment on a variable length track. Nevertheless,

building the theory under all three assumptions would be overly simplistic. Thus we replace the last two assumptions by assuming that appropriate path integration (PI) system is in place and provides the input to the model presented herein.

Behavioral studies showed the existence of PI system in mammals (Mittelstaedt & Mittelstaedt, 1980) and PI happens at least partially outside of the hippocampus (Alyan et al., 1997). On the other hand, the hippocampus is involved in the navigation based upon integration of idiothetic information, since a fornix lesion disrupts this type of navigation (Whishaw & Gorny, 1999). A PI system by definition should accommodate for changes in an animal's velocity and direction, and provide some measure of distance between the place where the trial started and the current location of the animal. Such a spatial output is similar to the output of a time integration system that records the time between the trial onset and current moment.

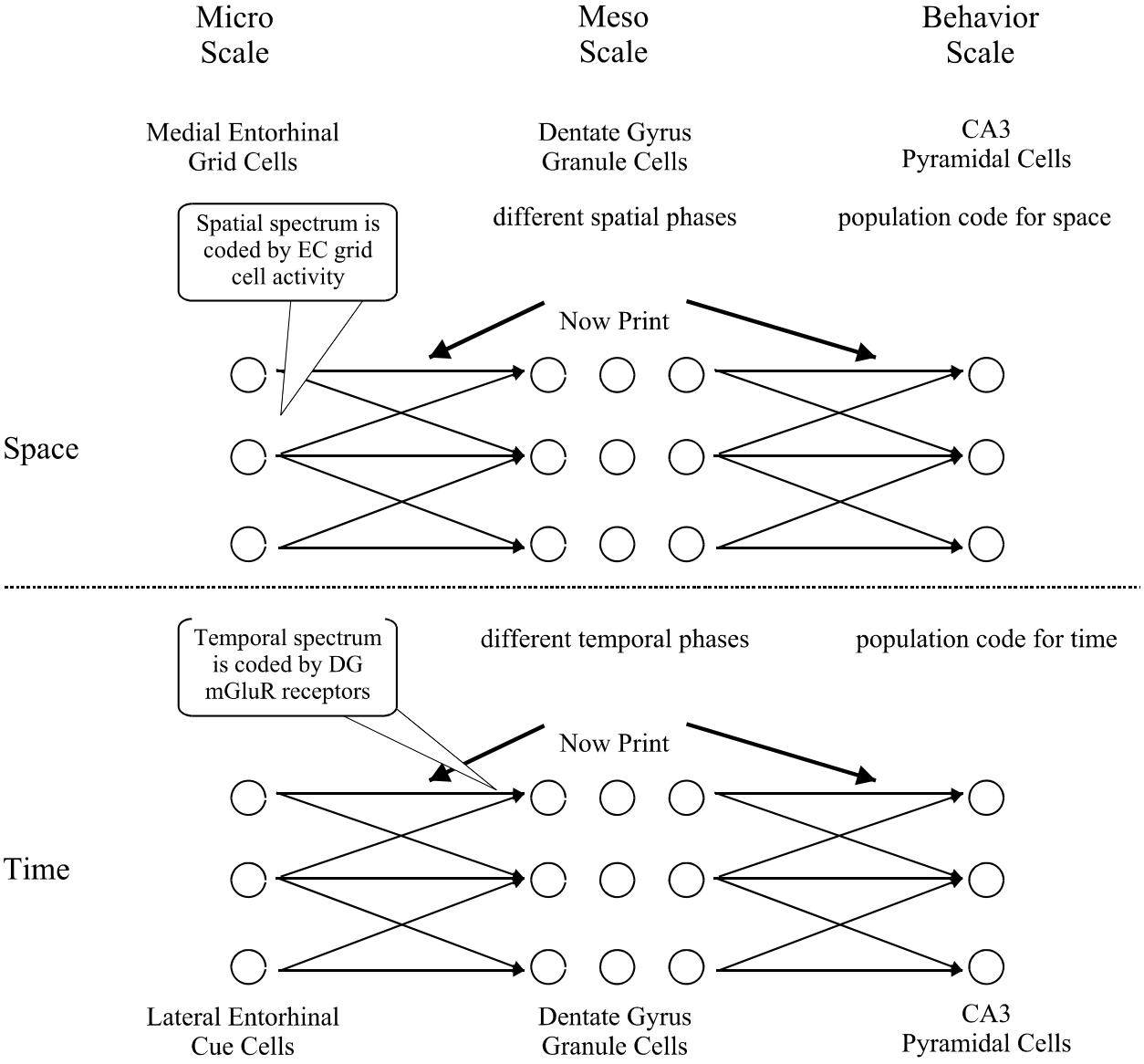

Figure 1. Homologous entrorhinal-dentate-CA3 circuits for spatial and temporal processing. See text for details.

Spectral Timing. Both spatial and temporal representational systems need to solve the following problem. The brain builds representations and guides the behavior over spatial scales of many meters and temporal scales of many seconds, while many individual neurons operate on much smaller spatial and temporal scales. One approach to solving this problem is to use a population code for space and time that combines a limited number of integrators with fixed but different spatial or temporal periods. These fixed periods can span a *spectrum* of spatial or temporal scales, and indeed the Grossberg et al model of adaptively timed learning is called the *spectral timing model*. This paper investigates how a representation of space that is much larger than any individual scale of the spectrum can be built by combining several spatial scales in a manner that strikingly resembles the circuitry that has been proposed for spectral timing; see Figure 1.

In the spatial domain, the recent exciting discovery of grid cells in the entorhinal cortex (EC) by Hafting et al. (2005) casts a new light on the input signal that can lead to adaptive formation of the large behavioral scales that are needed for navigation. This paper shows how a proper combination of multiple scales of grid cells leads to formation of hippocampal place cells through two stages of converging inputs as shown in Figure 1.

In the first stage of a spectral timing model, multiple cue cell outputs from the entorhinal cortex converge on cells in the dentate gyrus. Different DG cells are tuned to respond to different temporal delays along a spatial gradient in a septo-temporal direction (Nowak & Berger, 1992). Such a gradient of temporal delays may be implemented within EC-DG projections by using a gradient of different Ca^{++} concentrations that influence metabotropic glutamate receptors (mGluR) across the cells in the gradient (Fiala, Bullock, & Grossberg, 1996; Grossberg & Merrill, 1992, 1996).

Spectral Spacing. An analogous gradient of spatial coordinates can be based on entorhinal grid cells. Hafting et al. (2005) reported that there exists a gradient of spatial periods, or scales, of grid cells in EC that is aligned with the dorso-ventral EC axis. Spatial scale increases from 40cm at the most dorsal recording sites to 70cm in the most ventral sites (Hafting et al., 2005). The dorso-ventral gradient of grid cells' periods instantiates the spectrum of spatial scales. To further clarify the analogy between the spatial and temporal model, note that there is a topology in the projections from EC to DG such that the dorsolateral band of EC projects more to the septal end of the DG while the ventromedial band of EC projects more to the temporal end of DG (Burwell & Amaral, 1998). Thus the dorso-ventral gradient in EC corresponds to the septo-temporal gradient in DG. Within each spatial scale, grid cells have various orientations of the grid and shifted grid positions. According to these results, for a specific orientation, about five evenly shifted grid cells are sufficient to cover the space without gaps. The model presented here thus uses five cells per spatial scale. This is represented in the sketch of the first stage of the spatial model in Figure 2. When the animal moves through the environment, different grid cells from each spatial scale are periodically active. Multiple grid cell outputs from the entorhinal cortex converge on cells in the dentate gyrus.

The spatial model outlined in Figures 1 and 2 can be called a *spectral spacing model* by comparison with its homologous spectral timing model. We show here how a spectral spacing model can, through a two stage entorhinal-dentate-CA3 network, expand the spatial scale of grid cells in a manner analogous to how the spectral timing model expands the temporal scale through its parallel entorhinal-dentate-CA3 network. Previous simulations (e.g. by Fuhs & Touretzky, 2006) showed that the combination of several spatial scales leads to a unique spatial representation over an expanded spatial interval much larger than the period of any of the

individual spatial scales of entorhinal grid cells. The spectral spacing model presented herein not only replicates these results, but also provides a first theoretical explanation of why and how this expansion occurs.

In the second stage of a spectral timing model, output of DG cells with a fixed preferred delay, or temporal phase, converge on hippocampal CA3 cells (see Figure 1) to form a full temporal spectrum that can span a behavioral time scale of hundreds of milliseconds or seconds. In the second stage of a spectral spacing model, DG cells with a fixed preferred spatial phase, as explained below, provide signals that converge on hippocampal CA3 cells to form a full spatial spectrum that can span a behavioral spatial scale of many meters.

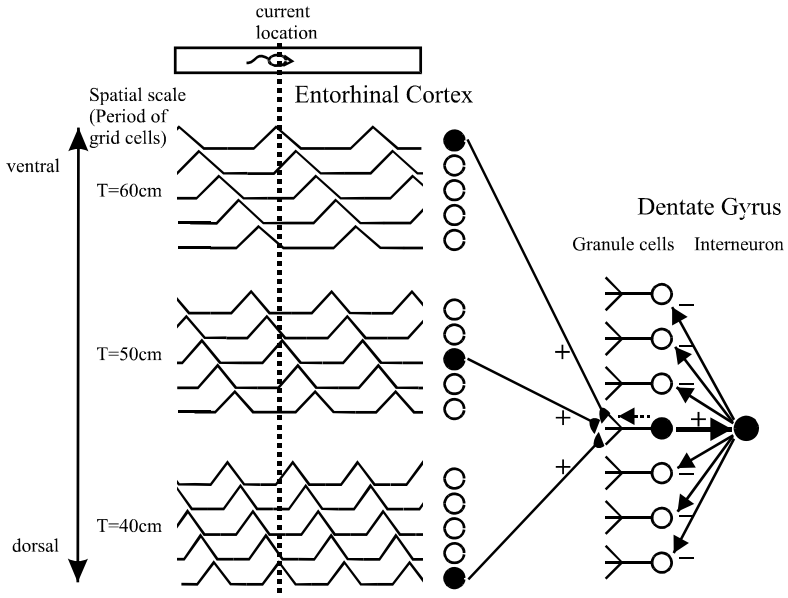

Figure 2. Model for place cell learning. 3 populations of entorhinal grid cells of 5 cells each are aligned along the dorso-ventral gradient in entorhinal cortex and have respective spatial scales. Their firing profiles are represented as peaks of corresponding activity trace and aligned with the track. The current location of the animal causes the corresponding grid cells to fire (filled circles). The dentate gyrus granule cell that receives strong projections from all three of the active grid cells fires in response to this input (filled circle) and activates the interneuron to suppress other granule cells. The back-propagating action potential in this granule cell (dotted arrow) triggers learning of projections from active entorhinal grid cells; cf. Grossberg (1975). For clarity, only currently active projections are shown.

Materials and Methods

Multiple Spatial Scales. Here we propose a mechanism for how dentate gyrus granule cells receive inputs from several nearby spatial scales in the entorhinal cortex and learn to combine these inputs to generate place cells that operate on a much larger spatial scale than individual grid cells. Fuhs and Touretzky (2006) showed to some extent that combining input from multiple spatial scales does lead to unique place fields. However, they did not analyze: (1) how the synaptic connectivity between grid cells and place cells can learn to combine spatial scales; (2) what is the maximal spatial expansion that can be achieved by combining certain scales; and (3) what is the theoretical foundation for this expansion. The model presented here proposes answers to these three questions.

Now Print Signals. In both spectral timing and spectral spacing systems, transient Now Print learning signals act at the dentate gyrus to selectively tune a subset of temporal or spatial phases. In the spatial model, the modulatory Now Print signal that enhances the synaptic modification is theta-bound and likely to be induced by cholinergic and GABAergic inputs from medial septum. Hasselmo, Bodelòn, and Wyble (2001) suggested, based on experimental data, how septal modulation can enhance spatial learning on a certain phase of the theta rhythm. In the temporal model, a Now Print signal can also be theta-bound, especially in the light of data on stimulus-evoked theta reset (Givens, 1996). The spectral timing model predicts that the temporal window during which a Now Print signal is effective is provided by metabotropic glutamate receptor (mGluR) dynamics (Fiala, Bullock, & Grossberg, 1996; Grossberg & Merrill, 1992; Ichise et al., 2000). Each of the fixed delays in the spectral timing model is proposed to be due to an mGluR burst that occurs at a different delay. These different delays are predicted to be determined by different calcium concentrations that are organized on a spatial gradient across the cells with different delays. If the homolog between temporal and spatial learning persists down to the biochemical level, then one would expect the temporal window during which a Now Print signal is effective in the spectral spacing model to also be determined by mGluR, but without different delays across cells. Indeed, spatial learning is disrupted by blocking mGluR (Balshun et al., 1999). The remainder of this paper analyzes the spectral spacing model, because the spectral timing model has previously been presented.

Least Common Multiple of Spatial Scales. As in the data of Hafting et al. (2005), EC grid cell activity for each spatial scale is a periodic process (Figure 2). The only difference between the scales is the period of this activity, and therefore, of the inputs to DG. Thus DG cells add several periodic processes $a_1 x_1(t) + a_2 x_2(t) + \ldots + a_n x_n(t)$ through synaptic integration. EC inputs could, in principle, be set up as a gradient of influences from different spatial scales, or as a set of equal influences for all scales (in the latter case $a_1 = a_2 = \ldots = a_n$). The period of the resulting process does not depend on these coefficients as long as they are non-zero; it only depends on periods of components and is equal to their *least common multiple* (e.g., see p.143 in Hartmann, 1997). As a result, the total space that can be covered by unique input combinations, and therefore unique representations, within a transversal DG slice is predicted to have the size of the least common multiple of the incoming grid periods. It will not depend on whether a gradient of influences or equal influences were used (the supporting simulation results with Gaussian profiles of influences normalized to match total input signal are not shown). For simplicity, this paper illustrates how an equal influence of spatial scales determines the resulting DG activity.

In the model simulations, different DG slices receive different combinations of nearby spatial scales. Suppose, for example, there are scales of 40, 50, 60, and 70cm along a dorso-ventral gradient in EC. Assume that the slice closer to the septal end of DG receives the three finest scales, while a slice of DG that is closer to the temporal end receives the three coarsest scales. Then the first DG population will expand space up to 6m (least common multiple of 40, 50, and 60cm), and the second population will expand it to 21m (least common multiple of 50, 60, and 70cm). Note that both of these numbers are still less than the maximal possible expansion for combining all four inputs (42m). On the other hand, there are now two spatial scales in two transverse slices of DG, which can be further used downstream in the hippocampus to support the gradient of place field sizes observed by Kjelstrup et al. (2006). There can also be some interaction between these scales in DG based on mossy cells that mainly project between different transverse slices (Patton & McNaughton, 1995).

From a mathematical point of view, the best spatial scales to combine in order to achieve the maximal space expansion would have periods equal to prime numbers. For example, the scales of 40, 50, and 60cm suggested above have total space coverage of 6m, while the nearby scales of 41, 53, and 59cm can cover up to 1.282km. On the other hand, if one uses five grid cells per spatial scale and three spatial scales, combining inputs from them will lead to only 5^3=125 place fields across this space. It is just as unlikely that the brain uses prime numbers or multiples of 10 as scale periods, so the grid cell periods are likely to attain intermediate values. The simulations below show that these intermediate values are capable of providing both space expansion and dense place field coverage over the expanded space.

The first two simulations compare DG activity resulting from inputs from two spatial scales of 40 and 50cm that can expand the spatial representation up to 2m, and inputs from two spatial scales of 44 and 52cm that can expand the space up to 5.72 m. The simulations used a 6m track so that both results can be accomplished within the same setup. An interneuron (basket cell) driven by the combined activity of all granule cells inhibits the granule cells (Patton & McNaughton, 1995). The general structure of the network is shown in Figure 2. Only two spatial scales (two populations of EC grid cells) were used in the simulations. An ideal result would be a unique DG firing pattern for every combination of entorhinal inputs. Such a result would achieve precise spatial localization on the expanded spatial interval.

Fixed Connection Weights. The first two simulations used prewired EC-DG connection weights. In the ideal case, each DG cell will have weights so that only one of the EC cells per spatial scale has a strong influence on DG cell activity. That can be represented as a weight set shown in Table 1a. In this example, the DG cell responds when the second cell fires in the 40cm scale (44cm for the second simulation) and the fourth cell fires in the 50cm scale (52cm for second simulation). There are 25 possible combinations of EC inputs, so 25 custom weight sets were crafted and preloaded into the EC-DG projections to 25 granule cells. The simulation was run for 30 simulated seconds over 6m linear track simulating motion from the leftmost end to the rightmost end at a constant speed of 20cm/s. This allows direct correspondence between spatial coordinates and time.

Learned Connection Weights. The third simulation tested whether the ideal weights used in the first two simulations can emerge in the brain from a competitive learning process (Grossberg, 1976, 1978; Kohonen, 1984; Rumelhart & Zipser, 1988). For this simulation, two DG slices that consisted of 125 granule cells each to allow some redundancy. Each slice received input from the same spatial scales as in simulation 2, but the inputs to the second slice were spatially shifted by 30cm relative to inputs to the first slice. This was done to illustrate the idea of different spatial phases discussed above. The initial synaptic weights of EC-DG projections were generated randomly on the all-to-all basis. An example of a set of random weights is shown in Table 1b. These weights were updated during the simulation according to a spike-timing dependent plasticity rule with postsynaptically gated decay (Gorchetchnikov, Versace, & Hasselmo, 2005; Grossberg, et al., 2002). Several runs through the track were completed until the weight change during a single run fell below 5% for all weights. Cells with firing rates below 0.1Hz were discarded from analysis. For the rest of the cells the spatial information per spike was calculates using the equation $Information = \sum_i p_i R_i \log_2 R_i$ that Jung and McNaughton (1993) used for the analysis of the experimental results. The track was divided into 5cm bins, R_i is the ratio of firing rate within bin *i* to the average firing rate, and p_i is the probability of the animal being in bin *i*.

a)

Spatial Scale	Grid cell index				
	1	2	3	4	5
40(44)	0.05	0.9	0.05	0.05	0.05
50(52)	0.05	0.05	0.05	0.9	0.05

b)

Spatial Scale	Grid cell index				
	1	2	3	4	5
44	0.167	0.158	1.010	0.499	0.479
52	0.857	0.963	0.194	0.333	0.558

c)

Spatial Scale	Grid cell index				
	1	2	3	4	5
44	0.050	0.050	**0.950**	0.111	0.050
52	0.082	**0.986**	0.114	0.050	0.050

Table 1. (a) Pre-wired ideal synaptic weights for EC-DG projections for a single granule cell. (b) Random synaptic weights for EC-DG projections for a single granule cell. (c) Synaptic weights for EC-DG projections after fourth run for the same granule cell as in panel (b). Boldface highlights the two inputs that drive place field activity in this cell (double peak field 12 in Figures 3d and 3e).

Cellular dynamics were modeled with the KInNeSS software package (available for download at *http://www.kinness.net*) using conventional compartmental membrane equations described in the Appendix as well as elsewhere (Gorchetchnikov & Hasselmo, 2005). The precise sets of currents and parameters for each population are provided in the Appendix.

Results

The results of the first and second simulations are presented in Figures 3a-d. They show that the periodicity of the model dentate granule cell activities follow the theoretically calculated period. Only 10 out of 25 cells show place fields for entorhinal input with periods 40 and 50 cm (Figure 3b). All 25 cells show place fields when fed with entorhinal input with periods of 44 and 52cm (Figure 3d). One fifth of these place fields (fields 3, 10, 12, 19, and 21) show two peaks in different parts of the track. In both simulations, place fields cover about half of the space; the other half is filled with single spikes of various granule cells. The average firing rate for cells in the first simulation is 0.43Hz for cells that have place fields, 0.2Hz for cells that do not show place fields, and 0.3Hz overall. The firing rate within a place field is 10Hz, driven by the 10Hz theta rhythm-bound entorhinal input. The average firing rate for cells in the second simulation is 0.335Hz, and the average firing rate within a place field is 10Hz.

The results of the third simulation are presented in Figure 3e and 3f. The simulation was stopped after the fourth run because the change in synaptic weights fell below the criterion. In the first slice (Figure 3e) 21 out of 25 place fields that were shown during the prewired simulation were replicated after learning. However, four place fields shown during the second simulation were not learned and are marked in Figure 3e by black crosses. All four undeveloped place fields were single-peaked. Seven of the place fields that had single peaks during a prewired run developed second peaks during learning (fields 1, 7, 8, 15, 16, 18, and 24). Due to a

redundant number of granule cells, often different cells developed the same place fields (for example 12 cells developed place field 1). Table 1c shows the synaptic weights that evolved through learning after 4 runs, starting from the initial random weights shown in Table 1b. Most of the space not covered by place fields in the first slice (yellow bars in Figure 3e and 3f) was covered by place fields in the second slice.

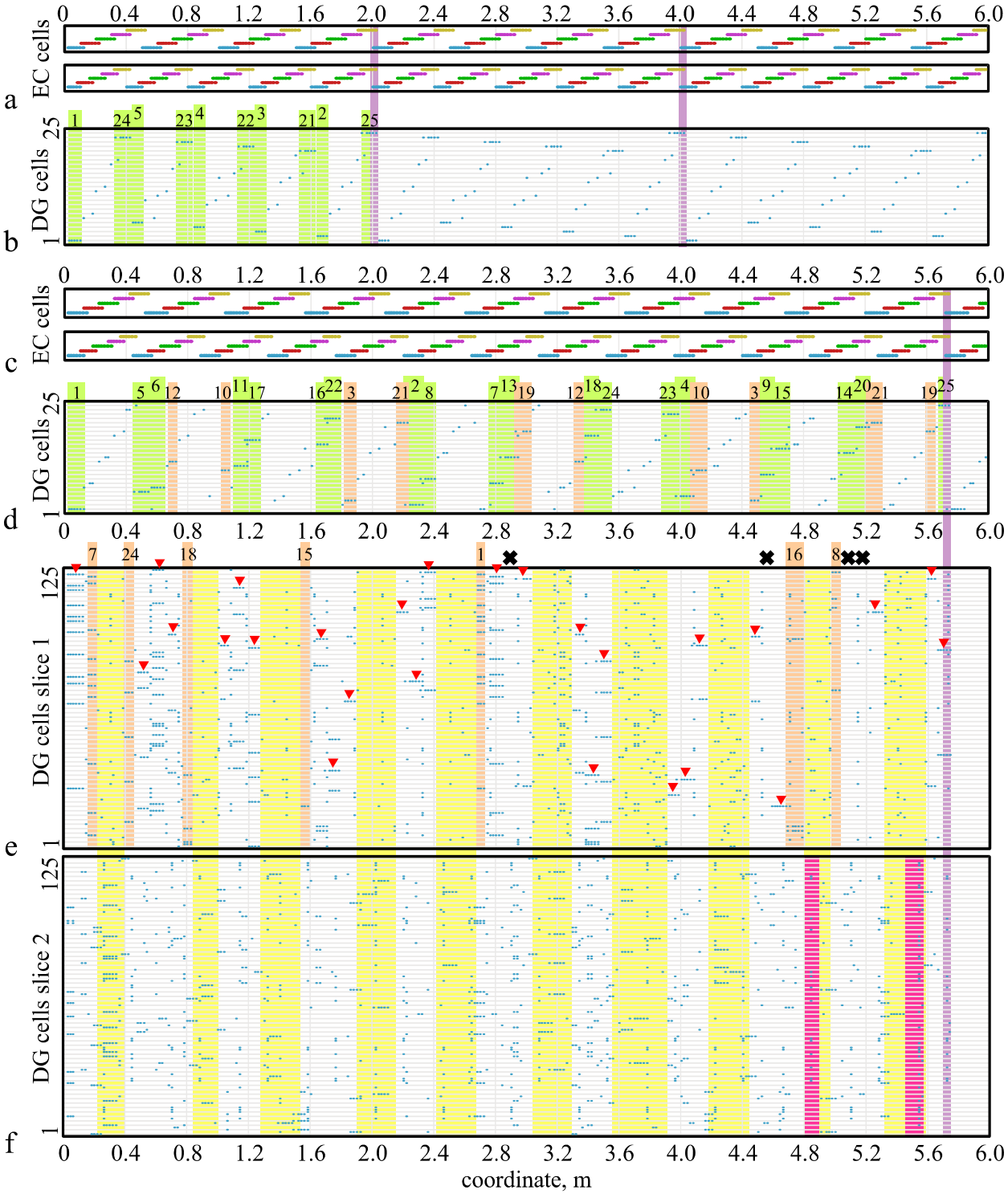

Figure 3. Simulation results: panels (a) and (b) refer to the first simulation; panels (c) and (d) refer to the second simulation, panels (c), (e) and (f) refer to the third simulation. (a) Activity for EC input with periods of 40cm and 50cm used in the first simulation. (c) Activity for EC input with periods of 44cm and 52cm used in the second and third simulations. (b), (d), (e), and (f): Spiking activity of dentate granule cells in the first, second, and third (e and f) simulations, respectively. Light purple vertical bars show the theoretical limit of space expansion. Light green vertical bars show single peak place fields. Light orange vertical bars show double peak place fields. Numbering of place fields in (b) and (d) correspond to the cell number in the population. Red triangles in (e) point to learned place fields that correspond to prewired place fields in (d). Black crosses mark prewired place fields in the second simulation that did not develop through learning. Orange bars with numbers in (e) show additional second peaks that developed through learning for place fields that had single peak in prewired case. The number next to the bar corresponds to the number of the original place field. Yellow bars in (e) and (f) correspond to the space that is not covered by place fields in (d) and (e). Red bars in (f) highlight parts of these areas that were not covered by the second DG slice.

For the cells in the third simulation the average firing rate is 0.339±0.097Hz during run 1 and 0.363±0.071Hz during run 4, which is an insignificant increase in firing rate as a result of learning. Average spatial information per spike did not change during learning (4.04±0.65 during run 1, 4.04±0.55 during run 4), but became more consistent as shown by reduction of standard deviation. Maximal firing rate inside individual bins was taken as a maximal firing rate inside the place field of the cell. It was 8.69±3.14Hz on average and reaching 12Hz for about one third of the cells. Place fields were on average 2.32 bins long before learning and 2.23 bins long after learning.

Discussion

The results of the first two simulations show that the spatial expansion was performed according to theoretical predictions. In the case of 40 and 50cm spatial scales, only 10 cells have reliable place fields, while with scales 44 and 52cm, all 25 cells had reliable place fields. In both cases, only about one-half of the expanded spatial interval was covered by place fields, while the other half was only marked by individual spikes that can be considered spontaneous firing. Since the size of place fields in the model approximately corresponds to the size of the entorhinal grid cell field with the smallest scale (about 10cm), this space coverage can be used to calculate the number of grid cells and spatial scales that are needed to cover a specific space. For example, combining three spatial scales leads to 125 possible input combinations, which can result in 125 place fields of about 10cm each. Therefore, these fields can cover 12.5m of space, which will be half of the expanded interval. Thus, the three spatial scales to be combined should have a least common multiple around 25m for the maximal efficiency of the model.

Multiple spatial phases. How can the model cover both halves of the expanded interval? The third simulation showed how two transverse slices in DG can be combined to cover the whole environment with place fields, even though each individual slice only covers half of the environment. In other words, two DG slices provide two phases of the spatial code and CA3 can combine these phases in a population code for an expanded spatial interval. Combining the activity from these two slices through convergence of DG-CA3 projections leads to complete coverage of the space by DG input to CA3 cells. In simulation 3, the only places that remained uncovered are places where place fields were supposed to be developed, but did not emerge

during learning, such as fields marked with black crosses in the first slice (Figure 3e) or by red bars in the second slice (Figure 3f).

Multi-peaked Dentate Gyrus Place Fields. The double-peak place fields in simulations 2 and 3 correspond to data recorded by Jung and McNaughton (1993) showing a significant fraction of multi-peaked dentate gyrus place fields. While these multiple peaks seem to be at odds with the idea of unique spatial representation that this paper proposes, this is not really the case. Again, addition of another DG slice to the network can resolve the ambiguity of multiple peaks. If a second slice combines two other spatial scales, both of the slices would probably have multi-peaked place fields. On the other hand, due to the difference in input spatial scales to these slices, it is highly unlikely that both peaks of the same place field in one slice will coincide with both peaks of some multi-peaked place field in another slice. As a result, through the convergence of inputs from these two slices in CA3, different CA3 cells will be active for different peaks of the same DG place field. Theoretically, the more slices one adds to the model, the higher the chances that the total population activity of DG cells is able to provide unique spatial coding over an arbitrary length of the track. Thus the next step in model development is to expand the network to include more than two spatial scales, multiple DG slices, and to converge the output of these slices onto a CA3 population.

What and Where in Context-Dependent Place Cells. Based on the experimental data, Doboli, Minai, and Best (2000) proposed that the DG plays a role in forming context-dependent place representations in the hippocampus. This suggestion is explicated by the model presented here. Grid cells are found in the more medial part of the entorhinal cortex, which receives input through postrhinal cortex (Burwell & Amaral, 1998) from the visual areas that represent the cortical "where" stream. At the same time, lateral entorhinal cortex receives inputs through perirhinal cortex (Burwell & Amaral, 1998) from temporal visual areas that represent the cortical "what" stream, and thus is a good candidate for providing contextual input to DG. Such input to granule cells will provide contextual information and lead to context-dependency and remapping of DG representations even when spatial input from grid cells does not change.

Comparing DG Simulations and Data. The firing rate of the model DG cells outside of the main place field is low and comparable with the spontaneous firing rate of these cells recorded experimentally (Jung & McNaughton, 1993). The model predicts that this rate is not truly spontaneous: a positive correlation should exist between firing of cells outside of their place fields and the activity of grid cells that are active when the animal is in the place field. This prediction follows from the size of overlap between firing of grid cells in different spatial scales. For example, in Figure 3c, yellow cells in both spatial scales have a long overlap of their activities at about 5.6-5.7m that results in a place field 25 in Figure 3d, but these cells also have much shorter overlaps of activity at about 0.45, 2.6, and 3.1m, which result in individual spikes in Figure 3d that can be considered as spontaneous by an outside observer.

Firing properties of DG granule cells in the simulations roughly correspond to properties recorded experimentally by Jung and McNaughton (1993, see their Table 1). In their recordings the diameter of DG place field was around 2.8 bins or 14.7cm. In the simulations presented here, the length of place field is around 2.23 bins or 11.15cm. Number of place fields per cell recorded experimentally was 1.79±1.4. Simulation 3 provided the number of place fields per cell as 1.41±0.64 after learning. The smaller size of field and smaller number of multipeak fields in the simulations is due to the simplicity of simulated network comparing to the real dentate gyrus. It also leads to a higher information value per spike in simulations (4.04±0.55 bits/spike vs 2.36±1.17 in experiments). Note that Jung and McNaughton used an additional time-shifting

paradigm to get rid of the noise in the data, and this paradigm further reduced their information scores. Finally, model development of the two-dimensional map case will also likely entail the reduction of the information value per spike.

Place Fields in DG, CA1, and CA3. Simulation 3 illustrates that the mechanism suggested here can be achieved through a self-organization process in EC-DG projections. Moreover, this process does not have to be limited to EC-DG projections; a similar process can take place in direct EC-CA1 projections. CA1 has much smaller number of cells than DG, which will lead to a larger number of entorhinal inputs per CA1 cell and a less precise spatial representation in CA1 than the one shown here. This property corresponds to data showing that place fields exist in CA1 after DG-CA3 lesion, but these fields are less precise than their normal counterparts (Brun et al., 2002).

How Do Grid Cells Arise? From Path Integration to a Resettable Grid Cell Map. As discussed so far, the model proposes how the limited spatial scales of grid cells can be expanded into a large-scale representation of space, but did not explain why grid cells have limited spatial scales in the first place. Spatial representation in the hippocampus has been shown to be disrupted by manipulations of the proprioceptive system (Calton et al., 2003). Furthermore, proprioceptive input allows navigation without sensory cues, notably homing behaviors based on path integration (Mittelstaedt & Mittelstaedt, 1980). In the absence of sensory cues, path integration (PI) inputs provide a "ground truth" upon which the computation of present location can build. PI has a limited spatial capacity, and must be reset periodically. Thus the output of the PI system must be periodic, leading to the periodic property of grid cells. The model's learned mapping from grid cells into hippocampal place cells then expands the spatial representation of the grid cell computation. Homologs of the PI to grid cell integration-to-map process are proposed to exist in other brain systems, as summarized below.

The key question that PI system design must answer is how a scalar signal that accumulates with path-integrated distance can be converted into a spatial map whose position of maximal activation changes with the distance traversed? In particular, suppose that a scalar signal is integrated from the outputs of animal proprioceptors as the animal moves through an environment. How can this scalar signal be converted into a map representation of space?

The model predicts that this is accomplished using the same strategy that has been used by the brain to generate other spatial brain maps that convert scalar inputs into a positional shift across a spatial map, namely a Position-Threshold-Slope (PTS) model. In particular, the model predicts that both the thresholds and the slopes (or sensitivities) of the grid signal functions increase from one side of the map to the other, and that the responses of the grid cells to these inputs are sharpened by an on-center off-surround network (Figure 4). If this hypothesis is confirmed by future experiments, then the grid cell representation can be viewed as a particular case of a general brain design.

The PTS hypothesis was first used to derive a spatial map from an analog scalar signal by Grossberg and Kuperstein (1989) in their model of saccadic eye movement control, which is another example of a "where" cortical stream process. Neurophysiological data wherein thresholds and slopes covary across cells involved in eye movement control have been reported by several investigators (Luschei & Fuchs, 1972; Robinson, 1970; Schiller, 1970). The same sort of network design was later used by Grossberg and Repin (2003) to explain how an analog spatial map for numerical representation is created in the parietal cortex, which is yet another "where" cortical stream process (Naccache & Dehaene, 2001; Rickard et al., 2000).

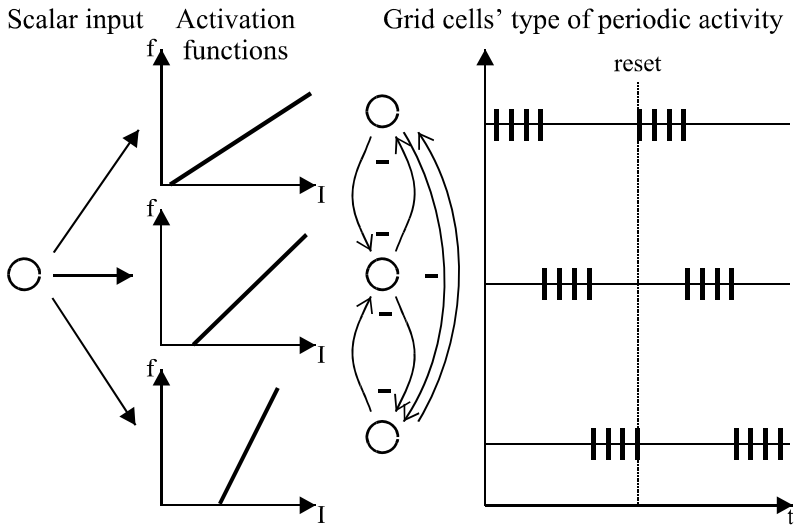

Figure 4. Position-Threshold-Slope (PTS) model. A scalar input on the left is provided to three cells whose signal functions have increasing thresholds and slopes that activate a contrast-enhancing on-center off-surround network. Increases in the scalar input selectively activates cells across a spatial map, which are periodically excited when the scalar input is reset through time. See text for further details.

Interaction between Position, Threshold, and Slope converts an accumulating input into a shift across the spatial map in the following way (see Figure 4). The scalar input excites all cells equally. A small input can strongly activate only cells whose signals have low thresholds. As the input continues to accumulate, the cells that have low thresholds fire more vigorously. However, cells with somewhat higher thresholds also start to fire. In addition, the *rate* of firing by cells with higher thresholds overtakes and exceeds that of the cells with lower thresholds, because the *slopes* of their signal functions are larger, even though their thresholds are also larger. As cells with higher thresholds become activated, they suppress the activity of the cells with lower thresholds through on-center off-surround interactions. As the input increases even further, the cells with even higher thresholds start to fire more than all the others. And so on. The location of the maximally activated cells hereby shifts across the map as the input accumulates (Grossberg & Kuperstein, 1989; Grossberg & Repin 2003). Because larger inputs can activate cells with both smaller and larger thresholds, the spatial span of active cells can increase with input amplitude even as the peak response shifts to the right. In order to control this distributed activation pattern, competitive interactions between the cells, notably on-center off-surround interactions among cells that obey membrane equations, respond to the inputs received through the array of signal functions by normalizing and spatially sharpening them into mode localized responses (Grossberg, 1973, 1980).

As in the case of analog numerical representation, such a spatial map has a limited spatial extent in which it can accurately represent its analog signal. In the case of numerical representation, this limitation leads to properties such as the Number Size effect (Dehaene, 1997; Grossberg & Repin, 2003). The path integration signal must therefore be *reset* when a maximal path integration size is reached, in order to preserve the accuracy of the map. After reset, path integration begins again as the animal continues to move through the environment, leading to the striking periodic activation pattern that is characteristic of grid cells.

Given that the conversion of scalar path integration signals into grid spatial representations has a limited spatial capacity, the brain needed to find a way to expand this spatial representation to enable effective navigation over terrains of terrestrial size. The multiple-scale self-organizing map that is described above provides such a way.

In summary, it may be that an iteration of two often used circuit designs (PTS maps and self-organizing maps) give rise to the basic grid and place cell profiles in response to path integration signals. Interestingly, the parietal map of numerical representation also faces the problem of how to extend its small numerical capacity to large numbers. Grossberg and Repin (2003) propose an explanation for how the brain uses the basic analog number map to learn place-value number systems that have an unlimited capacity.

Visual Landmarks and their Influence on Grid Cells via Hippocampal-to-Entrorhinal Feedback. Previous work on spectral timing has shown how correct timing of a response can be learned using DG-CA3 interactions, such that the DG provides a spectrum of timings over a range of delays, thereby enabling task-appropriate behavioral timing to be learned by the network using a cue-driven process that is modulated by reinforcement (Grossberg & Merrill, 1992, 1996; Grossberg & Schmajuk, 1989). In the case of spectral spacing, the DG provides a spectrum of grid-based spatial coordinates that can be used to learn place codes capable of spanning a large behaviorally-appropriate space. This space can, in turn, be organized with respect to landmarks and reward locations by a cue-driven process, much as in the case of spectral timing.

How is learning in this neural system stabilized through time? That is, how is the *stability-plasticity dilemma* solved, and catastrophic forgetting of the map prevented (Grossberg, 1980; Raizada & Grossberg, 2003)? Typically, this is done via top-down, modulatory on-center off-surround matching signals which, in the present case, would be carried from hippocampal place cells to the grid cells. Such feedback signals can modulate the activity of grid cells based upon which place cells are active. Place-to-grid feedback illustrates how visual landmarks can modulate the activity of both grid and place cells, whose primary activation is derived from path integration signals. Future studies will attempt to characterize this spatial cue-driven process using a unified framework in which two widely studied functions of the hippocampus, namely spatial and temporal processing, are combined and shown to benefit from homologous circuitry.

Appendix

Entorhinal cell description

At this point of model development, EC grid cells are just input generators that provide bursts of spikes to DG granule cells. These bursts are tuned to represent grid cell activity.

DG granule cell description

DG granule cells in the model consist of two compartments: soma and dendrite. This two-compartmental structure increases the integration time for synaptic inputs from EC to dendrites, and makes the inhibition to the soma relatively faster and more effective than the excitation to the dendrites. This improves the competitive interactions between DG cells.

The *somatic potential* is calculated according to

$$C_M \frac{dV_i^S}{dt} = -g_L V_i^S + g_A\left(E_A - V_i^S\right) + g_D^S\left(V_i^D - V_i^S\right) + I_i^Q + w_{inh} g_{qi}^I \left(E^I - V_i^S\right), \qquad (1)$$

where C_M is the membrane capacitance, V_i^S is the somatic potential of the cell *i*, g_L is the leakage conductance, g_A and E_A are the AHP conductance and reverse potential, respectively, g_D^S is the diffusion coefficient from dendrite to soma, V_i^D is the potential in the dendrite of the cell *i*, I_i^Q is the quadratic integrate-and-fire representation of currents producing a spike, and the last term is the synaptic inhibition from an inhibitory interneuron so that E^I is a reversal potential of the inhibitory GABA channel, g_{qi}^I is a channel conductance controlled by presynaptic action potentials of the interneuron (cell *q*), and the synaptic weight w_{inh}, which roughly corresponds to billions of channels per cm^2 of the membrane.

The *dendritic potential* is calculated according to

$$C_M \frac{dV_i^D}{dt} = -g_L V_i^D + g_D^D\left(V_i^S - V_i^D\right) + \left(E^E - V_i^D\right)\sum_j g_{ji}^E w_{ji}, \qquad (2)$$

where C_M is the membrane capacitance, V_i^D is the dendritic potential of the cell *i*, g_D^D is the diffusion coefficient from soma to dendrite, V_i^S is the potential in the soma of the cell *i*, g_L is the leakage conductance, and the last term is the synaptic excitation from EC cells with E^E the reversal potential of the excitatory AMPA channel, g_{ji}^E a channel conductance controlled by presynaptic action potentials of the EC cell *j*, and w_{ji} is the synaptic weight of the projection from entorhinal cell *j* to DG cell *i*.

Both diffusion coefficients g_D^S and g_D^D are calculated as shown for a generic coefficient g_D^z from *z*-th compartment's diameter d_z and length l_z, and axial resistance R_A^{SD} between soma and dendrite, which is identical for both compartments:

$$g_D^z = \frac{d_z}{4 l_z^2 R_A^{SD}}. \qquad (3)$$

Both g_{qi}^I and g_{ji}^E are controlled by the presynaptic action potential as summarized below for a generalized synaptic conductance g_z. Note, that g_z only provides the shape of synaptic conductance, while its magnitude is determined by the maximal conductance of the channel $\bar{g}$, and its timing is determined by a time t_z that is reset to zero by the arrival of the presynaptic action potential to this particular synapse. Note also, that this time reset includes axonal delay on the way to this synapse, so a presynaptic spike in the soma will arrive at different axonal terminals made by the same cell at different times, and as a result will cause a shift in time for the respective postsynaptic potentials.

$$g_z = \begin{cases} \dfrac{\bar{g}p}{\tau_f - \tau_r}\left(e^{-\frac{t_z}{\tau_f}} - e^{-\frac{t_z}{\tau_r}} \right) & if \quad \tau_r \neq \tau_f \\ \bar{g}\dfrac{t_z}{\tau_f} e^{1-\frac{t_z}{\tau_f}} & otherwise \end{cases}, \tag{4}$$

where $\bar{g}$ is the maximal conductance of the channel, τ_r and τ_f are rise and fall synaptic time constants, respectively, and t_z is the time since an action potential in the z-th axonal terminal between presynaptic and postsynaptic cells; and p is a scaling coefficient that enforces

$$\max\left(\frac{p}{\tau_f - \tau_r}\left(e^{-\frac{t_z}{\tau_f}} - e^{-\frac{t_z}{\tau_r}} \right) \right) = 1. \tag{5}$$

The conductance for the AHP current g_A is also calculated according to equations (4) and (5), except that the triggering spike in this case is produced by the same cell and there is no transmission delay.

Entorhinal-to-Granule Cell Learning. The synaptic weights from entorhinal cells to granule cells were preset in simulations one and two to the values such that a single granule cell has one strong weight from each of the spatial scales. An example of these weights is shown in Table 1a. In simulation three these weights were set initially to random values from a uniform distribution on the interval [0, 1.1]. An example of these random weights is presented in Table 1b. Learning is carried out by a postsynaptically gated learning equation. Variations of such gated learning equations have been used in many applications since they were introduced by Grossberg and his colleagues (e.g. Grossberg, 1974; Grossberg, Hwang, & Mingolla, 2002). They were applied to STDP learning by Gorchetchnikov, Versace, and Hasselmo (2005), and used here as:

$$\frac{dw_{ji}}{dt} = \lambda f_G\left(V_i^S\right)\left(g_{ji}^E f_N\left(V_i^S\right)\left(\hat{w} - \breve{w}\right) + w_0 - w_{ji}\right), \tag{6}$$

where λ is the learning rate, and $f_G\left(V_i^S\right)$ gates the learning process by a non-negative function of the postsynaptic signal V_i^S, where

$$f_G\left(V_i^S\right) = \left(V_i^S\right)^2. \tag{7}$$

By equation (6), w_{ji} tracks the spike-timing correlation $g_{ji}^E f_N\left(V_i^S\right)$ of presynaptic and postsynaptic signals, where g_{ji}^E obeys equation (4) and

$$f_N\left(V_i^S\right)=\begin{cases} D+1 & if \quad V_i^S \geq V_i^\theta \\ 10(t-s)+D+1 & if \quad s < t < s-0.1\,ms \\ \dfrac{-D}{25}\left(t-s+0.1\,ms\right)+D & if \quad s-0.1\,ms \leq t < s-25.1\,ms \\ 0 & otherwise \end{cases}. \tag{8}$$

In equation (6), $\hat{w}$, $\check{w}$, and w_0 (maximal, minimal, and baseline weights, respectively) scale the w_{ji} response. In equation (8), V_i^θ is the spiking threshold potential, *t* is time, *s* is the moment of the postsynaptic spike, and $D=\left(\check{w}-w_0\right)/\left(\hat{w}-\check{w}\right)$.

Action Potentials. Action potential generation was modeled with a quadratic integrate-and-fire (IAF) equation. This equation is a reduction of the classical Hodgkin-Huxley model (Hodgkin & Huxley, 1952) that includes fast sodium, delayed rectifier potassium, and leakage currents. The quadratic IAF equation was derived through a Taylor expansion of the original system by Ermentrout and Kopell (1986). Izhikevich (2004) provided a detailed comparison of quadratic IAF to other methods of spike generation. The specific version used in the model presented here was described previously by Gorchetchnikov and Hasselmo (2005):

$$I_z^Q = s_z\left(V_z^2 - V_z V_z^\theta\right), \tag{9}$$

where V_z is the somatic membrane potential, V_z^θ is the spiking threshold potential, and parameter s_z has the dimension of $\frac{mS}{mV\cdot cm^2}$ for consistency with other equations.

DG interneuron description

The DG interneuron (basket cell) in the model consists of a single compartment where the membrane potential is calculated according to

$$C_M\frac{dV_q}{dt} = -g_L V_q + I_q^Q + w_{exc} g_q^E\left(E^E - V_q\right), \tag{10}$$

where C_M is the membrane capacitance, V_q is the somatic potential of the interneuron (index *q* is used to distinguish interneuron potentials and currents from granule cells potentials and currents), g_L is the leakage conductance, I_q^Q is the quadratic integrate-and-fire representation of currents producing a spike, and the last term is the synaptic excitation from granule cells so that E^E is a reverse potential of the excitatory AMPA channel, g_q^E is a channel conductance controlled by presynaptic action potentials of granule cells, and w_{exc} is the constant synaptic weight of projections from granule cells to the interneuron.

* * *

The parameter values used in simulations are summarized in Tables A1 and A2. Note, that in all equations, the cell's resting potential is chosen to be *0mV*; thus for conventional

neurophysiological voltage notation, $60mV$ should be subtracted from parameters listed in Tables A1 and A2.

Parameter	Used in equations	Value
C_M (membrane capacitance)	(1), (2), (10)	$1\mu F/cm^2$
E^E (AMPA reverse potential)	(2), (10)	$+60mV$
E^I ($GABA_A$ reverse potential)	(1)	$-10mV$
E_A (AHP reverse potential)	(1)	$-30mV$
R_A (axial resistance)	(3)	$25kOhm \cdot cm$
λ (learning rate)	(6)	0.1
$\hat{w}$ (maximal weight)	(6), (8)	1.1
$\breve{w}$ (minimal weight)	(6), (8)	0
w_0 (baseline weight)	(6), (8)	0.05
w_{exc} (excitatory weight)	(10)	3
w_{inh} (inhibitory weight)	(1)	1

Table A1. Parameters of simulations that are used across all cells.

Parameter	Used in equations	Used in compartment	Value
τ_r (AMPA raise time constant)	(4), (5)	Interneuron soma	$2ms$
τ_f (AMPA fall time constant)	(4), (5)	Interneuron soma	$2ms$
$\bar{g}$ (exc maximal conductance)	(4)	Interneuron soma	$0.1pS$
τ_r ($GABA_A$ raise time constant)	(4), (5)	Granule cell soma	$1ms$
τ_f ($GABA_A$ fall time constant)	(4), (5)	Granule cell soma	$7ms$
$\bar{g}$ (inh maximal conductance)	(4)	Granule cell soma	$2.5pS$
τ_r (raise time constant)	(4), (5)	Granule cell dendrite	$11ms$
τ_f (fall time constant)	(4), (5)	Granule cell dendrite	$11ms$
$\bar{g}$ (exc maximal conductance)	(4)	Granule cell dendrite	$0.15pS$
τ_r (AHP raise time constant)	(4), (5)	Granule cell soma	$0.1ms$
τ_f (AHP fall time constant)	(4), (5)	Granule cell soma	$5ms$
$\bar{g}$ (AHP maximal conductance)	(4)	Granule cell soma	$2.5pS$
g_L (leakage conductance)	(10)	Interneuron soma	$0.01mS/cm^2$
g_L (leakage conductance)	(1)	Granule cell soma	$0.001mS/cm^2$
g_L (leakage conductance)	(2)	Granule cell dendrite	$0.2mS/cm^2$
d_S (somatic diameter)	(3)	Granule cell soma	$100\mu m$

l_S (somatic length)	(3)	Granule cell soma	$100\mu m$
d_D (dendritic diameter)	(3)	Granule cell dendrite	$10\mu m$
l_D (dendritic length)	(3)	Granule cell dendrite	$500\mu m$
V_q^θ (spiking threshold)	(9)	Interneuron soma	$20mV$
s_q (scaling of IAF)	(9)	Interneuron soma	$0.06\frac{mS}{mV \cdot cm^2}$
V_i^θ (spiking threshold)	(8), (9)	Granule cell soma	$30mV$
s_i (scaling of IAF)	(9)	Granule cell soma	$0.03\frac{mS}{mV \cdot cm^2}$

Table A2. Population-specific parameters used in simulations. Note that somatic passive leakage conductances for are reduced to compensate for additional leakage included in quadratic integrate and fire equation.

References

Alyan, S. H., Paul, B. M., Ellsworth, E., White, R. D., & McNaughton, B. L. (1997). Is the hippocampus required for path integration? Society for Neuroscience Abstracts, 23, 504..

Berger, T. W., Berry, S. D., & Thompson, R. F. (1986). Role of the hippocampus in classical conditioning of aversive and appetitive behaviors. In I. R. L., & P. K. H. (Eds.), The Hippocampus, Vol. 4, (pp. 203–239). New York, NY: Plenum Press.

Berger, T. W., & Thompson, R. F. (1978). Neuronal plasticity in the limbic system during classical conditioning of the rabbit nictiating membrane response, i: The hippocampus. Brain Research, 145, 323–346.

Berger, T. W., & Thompson, R. F. (1980). Hippocampal unit-behavior correlations during classical conditioning. Brain Research, 193, 229–248.

Brun, V. E., Otnæss, M. K., Molden, S., Steffenach, H.-A., Witter, M. P., Moser, M.-B., & Moser, E. I. (2002). Place cells and place recognition maintained by direct entorhinal-hippocampal circuitry. Science, 296, 2243–2246.

Burwell, R. D., & Amaral, D. G. (1998). Cortical afferents of the perirhinal, postrhinal, and entorhinal cortices of the rat. Journal of Comparative Neurology, 398, 179–205.

Calton, J. L., Stackman, R. W., Goodridge, J. P., Archey, W. B., Dudchenko, P. A., & Taube, J. S. (2003). Hippocampal place cell instability after lesions of the head direction cell network. Journal of Neuroscience, 23(30), 9719–9731.

Dehaene, S. (1997). The Number Sense: How the Mind Creates Mathematics. New York, NY: Oxford University Press.

Doboli, S., Minai, A. A., & Best, P. J. (2000). Latent attractors: A model for context-dependent place representations in the hippocampus. Neural Computation, 12(5), 1009–1043.

Eichenbaum, H., Dudchenko, P., Wood, E., Shapiro, M., & Tanila, H. (1999). The hippocampus, memory and place cells: Is it spatial memory or a memory space? Neuron, 23, 209–226.

Eichenbaum, H., Otto, T., & Cohen, N. J. (1994). Two functional components of the hippocampal memory system. Behavioral and Brain Sciences, 17, 449–472.

Ermentrout, G. B., & Kopell, N. J. (1986). Parabolic bursting in an excitable system coupled with slow oscillation. SIAM Journal of Applied Mathematics, 46, 233–252.

Fiala, J. C., Grossberg, S., & Bullock, D. (1996). Metabotropic glutamate receptor activation in cerebellar Purkinje cells as substrate for adaptive timing of the classically conditioned eye-blink response. Journal of Neuroscience, 16(11), 3760–3774.

Fuhs, M. C., & Touretzky, D. S. (2006). A spin glass model of path integration in rat medial entorhinal cortex. Journal of Neuroscience, 26(16), 4266–4276.

Gibbon, J. (1977). Scalar expectancy and Weber's law in animal timing. Psychological Review, 84, 279–325.

Givens, B. S. (1996). Stimulus-evoked resetting of the dentate theta rhythm: Relation to working memory. Neuroreport, 8, 159–163.

Gorchetchnikov, A., & Hasselmo, M. E. (2005). A biophysical implementation of a bidirectional graph search algorithm to solve multiple goal navigation task. Connection Science, 17(1-2), 145–166.

Gorchetchnikov, A., Versace, M., & Hasselmo, M. E. (2005). A model of STDP based on spatially and temporally local information: Derivation and combination with gated decay. Neural Networks, 18, 458–466.

Grossberg, S. (1973). Contour enhancement, short term memory, and constancies in reverberating neural networks. Studies in Applied Mathematics, LII, 213–257.

Grossberg, S. (1974). Classical and instrumental conditioning by neural networks. Progress in Theoretical Biology, 3, 51–141.

Grossberg, S. (1975). A neural model of attention, reinforcement, and discrimination learning. International Review of Neurobiology, 18, 263–327.

Grossberg, S. (1976). Adaptive pattern classification and universal recoding I: Parallel development and coding of neural feature detectors. Biological Cybernetics, 23, 121–134.

Grossberg, S. (1978). A theory of human memory: Self-organization and performance of sensory-motor codes, maps, and plans. Progress in Theoretical Biology, 5, 233–374.

Grossberg, S. (1980). How does the brain build a cognitive code? Psychological Review, 87, 1–51.

Grossberg, S., Hwang, S., & Mingolla, E. (2002). Thalamocortical dynamics of the McCollough effect: Boundary-surface alignment through perceptual learning. Vision Research, 42, 1259–1286.

Grossberg, S., & Kuperstein, M. (1989). Neural Dynamics of Adaptive Sensory-Motor Control: Expanded Edition. Elmsford, NY: Pergamon Press.

Grossberg, S., & Merrill, J. (1992). A neural network model of adaptively timed reinforcement learning and hippocampal dynamics. Cognitive Brain Research, 1, 3–38.

Grossberg, S., & Merrill, J. (1996). The hippocampus and cerebellum in adaptively timed learning, recognition, and movement. Journal of Cognitive Neuroscience, 8(3), 257–277.

Grossberg, S., & Repin, D. (2003). A neural model of how the brain represents and compares multi-digit numbers: Spatial and categorical processes. Neural Networks, 16, 1107–1140.

Grossberg, S., & Schmajuk, N. A. (1989). Neural dynamics of adaptive timing and temporal discrimination during associative learning. Neural Networks, 2, 79–102.

Hafting, T., Fyhn, M., Molden, S., Moser, M.-B., & Moser, E. I. (2005). Microstructure of the spatial map in the entorhinal cortex. Nature, 436(11), 801–806.

Hartmann, W. M. (1997). Signals, Sound, and Sensation. New York, NY: American Institute of Physics.

Hasselmo, M. E., Bodel´on, C., & Wyble, B. P. (2002). A proposed function for hippocampal theta rhythm: Separate phases of encoding and retrieval enhance reversal of prior learning. Neural Computation, 14, 1–25.

Hodgkin, A. L., & Huxley, A. F. (1952). Quantitative description of membrane current and its application to conduction and excitation in nerve. Journal of Physiology, 117, 500–544.

Hoehler, F. K., & Thompson, R. F. (1980). Effects of interstimulus (CS-UCS) interval on hippocampal unit activity during classical conditioning of the nictitating membrane response of the rabbit (Oryctolagus Cuniculus). Journal of Comparative and Physiological Psychology, 94, 201–215.

Ichise, T., Kano, M., Hashimoto, K., Yangihara, D., Nakao, K., Shigemoto, R., Katsuki, M., & Aiba, A. (2000). mGluR1 in cerebellar Purkinje cells essential for long-term depression, synapse elimination, and motor coordination. Science, 288, 1832–1835.

Izhikevich, E. M. (2004). Which model to use for cortical spiking neurons? IEEE Transactions on Neural Networks, 15, 1063–1070.

Jung, M. W., & McNaughton, B. L. (1993). Spatial selectivity of unit activity in the hippocampal granular layer. Hippocampus, 3, 165–182.

Kohonen, T. (1984). Self-organization and Associative Memory. Berlin: Springer-Verlag.

Luschei, E. S., & Fuchs, A. F. (1972). Activity of brain stem neurons during eye-movement of alert monkeys. Journal of Neurophysiology, 35, 445–461.

Mittelstaedt, H., & Mittelstaedt, M.-L. (1982). Homing by path integration. In F. Papi, & H. G. Wallraff (Eds.), Avian Navigation, (pp. 290–297). Berlin, Germany: Springer Verlag.

Naccache, L., & Dehaene, S. (2001). The priming method: Imaging unconscious repetition priming reveals an abstract representation of number in the parietal lobes. Cerebral Cortex, 11, 966–974.

Nowak, A. J., & Berger, T. W. (1992). Functional three-dimensional distribution of entorhinal projections to dentate granule cells of the in vivo rabbit hippocampus. Society for Neuroscience Abstracts, 18, 141.15.

O'Keefe, J. M., & Dostrovsky, J. (1971). The hippocampus as a spatial map. Preliminary evidence from unit activity in the freely-moving rat. Brain Research, 34(1), 171–175.

Patton, P. E., & McNaughton, B. L. (1995). Connection matrix of the hippocampal formation: I. the dentate gyrus. Hippocampus, 5(4), 245–286.

Raizada, R., & Grossberg, S. (2003). Towards a theory of the laminar architecture of cerebral cortex: Computational clues from the visual system. Cerebral Cortex, 13, 100–113.

Redish, A. D., Rosenzweig, E. S., Bohanick, J. D., McNaughton, B. L., & Barnes, C. A. (2000). Dynamics of hippocampal ensemble activity realignment: Time versus space. Journal of Neuroscience, 20(24), 9298–9309.

Rickard, T. C., Romero, S. G., Basso, G., Wharton, C., Flitman, S., & Grafman, J. (2000). The calculating brain: An fMRI study. Neuropsychologia, 38, 325–335.

Roberts, W. A., Cheng, K., & Cohen, J. S. (1989). Timing, light, and tone signals in pigeons. Journal of Experimental Psychology: Animal Behavior Processes, 15, 23–25.

Robinson, D. A. (1970). Oculormotor unit behavior in the monkey. Journal of Neurophysiology, 35, 393–404.

Rumelhart, D., & Zipser, D. (2005). Feature discovery by competitive learning. Cognitive Science, 9, 75–112.

Schiller, P. H. (1970). The discharge characteristics of single units in the oculomotor and abducens nuclei of the unanesthetized monkey. Experimental Brain Research, 10, 347–362.

Scoville, W. B., & Milner, B. (1957). Loss of recent memory after bilateral hippocampal lesions. Journal of Neurol Neurosurg Psychiatry, 20, 11–21.

Smith, M. C. (1968). CS-US interval and US intensity in classical conditioning of the rabbits nictitating membrane response. Journal of Comparative and Physiological Psychology, 91, 407–417.

Whishaw, I. Q., & B, G. (1999). Path integration absent in scent-tracking fimbria-fornix rats: Evidence for hippocampal involvement in “sense of direction” and “sense of distance” using self-movement cues. Journal of Neuroscience, 19(11), 4662–4673.

Acknowledgements

Stephen Grossberg was supported in part by the National Science Foundation (SBE-0354378) and the Office of Naval Research (N00014-01-1-0624). Anatoli Gorchetchnikov was supported by the National Science Foundation (SBE-0354378).